The Pennsylvania State University

The Graduate School

College of Engineering

LIFE ASSESSMENT OF A MINIATURE MICROWAVE-FREQUENCY ION THRUSTER

A Thesis in

Aerospace Engineering

by

Sang Chieh Hsieh

Submitted in Partial Fulfillment
of the Requirements
for the Degree of

Master of Science

August 2018

The thesis of Sang Chieh Hsieh was reviewed and approved* by the following:

Michael M. Micci
Professor of Aerospace Engineering
Thesis Co-Advisor

Sven G. Bilén
Professor of Engineering Design, Electrical Engineering, and Aerospace Engineering
Thesis Co-Advisor

Amy Pritchett
Professor of Aerospace Engineering
Head of the Department of Aerospace Engineering

*Signatures are on file in the Graduate School

ABSTRACT

This thesis presents an assessment of grid life for the Miniature Microwave-Frequency Ion Thruster (MMIT), which is being developed at The Pennsylvania State University. The MMIT is proposed mainly for use in station keeping, modest delta-V maneuvers, and attitude control on small satellites. Previous research on the MMIT developed a working prototype that demonstrated plasma generation, plasma sustainment, and ion beam extraction. The iterative development process has incrementally improved the MMIT. Findings from previous research on the arcing and sputtering of the grids drove us to establish a new design criterion for grid life. The main failure criterion for the grids depends on the mass loss of the grid.

Research on the thruster life can be divided into three parts: predicting the life of the grids, determination of the variables in the life equation, and proposing new design criteria based on the life assessment. We focus on studying the effective variables in the life prediction. Experimental data show the deformation of the grid caused by arcing and sputtering. The voltage difference between the grids serves to throttle the thruster and is the driver for sputtering. The influence of hole diameter and voltage on the life equation helps us understand how the arcing and sputtering affect life. Based on other research in the literature, we define a new parameter for the MMIT.

The correlation between hole diameter, acceleration voltage, and thrust gives us a new perspective on the grid design. Previous research designed the grid based on the thrust requirement alone. However, the grid life is also one of many aspects to consider. The findings on the hole diameter and grid material with propellant lead to new design criteria. The fully functional flight version of the thruster should combine the previous design standard and new design guidelines.

TABLE OF CONTENTS

List of Figures v

List of Tables vii

List of Symbols viii

Acknowledgments xi

Chapter 1 Introduction 1

1.1 Life Assessment 1
1.2 Thesis Overview 2

Chapter 2 Theoretical Background 3

2.1 Propulsion System 3
2.2 Rocket Propulsion 4
2.3 Electric Propulsion 5
2.3.1 Ion Thruster 5
2.3.1.1 Ionization 6
2.3.1.2 Acceleration 8
2.3.1.3 Neutralization 11
2.4 Previous Research in Penn State 11
2.5 Latest MMIT Research 14
2.6 Grid Erosion 15
2.7 Life Assessment Calculation of Grids 16

Chapter 3 Experimental Setup and Measurement Method 19

3.1 Vacuum Chamber System 19
3.2 MMIT System 20
3.3 Propellant and Extraction System 20
3.4 Measurement Method 21

Chapter 4 MMIT Design Criteria 22

4.1 Previous Design 22
4.2 Latest Design Overview of MMIT 23
4.3 Calculation of Grid Life 24
4.4 Experimental Findings 25
4.5 New Design Criterion 33

Chapter 5 Conclusions and Future Work 35

Bibliography 37

LIST OF FIGURES

Figure 2-1. Categories of propulsion systems....3

Figure 2-2. Forces acting on the control volume of a rocket engine[16] 4

Figure 2-3. Schematic of ion thruster[2] 6

Figure 2-4. Schematic of Kaufman thruster[16] 7

Figure 2-5. Schematic of radio-frequency ion thruster[17]....7

Figure 2-6. Schematic of Microwave-frequency ion thruster[18]....8

Figure 2-7. Space-charge effect 10

Figure 2-8. Trudel's MRIT (a) compared to a U.S. quarter (b) operational test in a vacuum chamber[19]....12

Figure 2-9. Lubey's MMIT operational test in a vacuum chamber[23]....12

Figure 2-10. (a) Lubey's MMIT[23], (b) Taunay's MMIT[24] 13

Figure 2-11. Taunay's MMIT operational test in a vacuum chamber, (a) single-hole grid configuration, and (b) extraction grid configuration.[24] 13

Figure 2-12. Asif's MMIT[26]....15

Figure 2-13. Asif's MMIT operating with different accelerating voltages[26] 15

Figure 2-14. Charge-exchange collision 16

Figure 3-1. Vacuum chamber and pumps 19

Figure 3-2. Schematic for microwave power injection into MMIT[26] 20

Figure 3-4. Schematic of measurement....21

Figure 4-1. Cross-section view of latest MMIT prototype[27] 23

Figure 4-2. Structural unit of MMIT....24

Figure 4-3. Hole diameter after operating....25

Figure 4-4. Center-to-center hole spacing after operating 26

Figure 4-5. Ion incident energy vs. sputtering yield for Xe on Mo 28

Figure 4-6. Experimental data of hole diameter vs. K 29

Figure 4-7. Hole diameter vs. K 30

Figure 4-8. Ion incident energy vs. net sputtering yield for Xe on Mo and Ar on Fe 31

Figure 4-9. Voltage vs. K 32

Figure 4-10. Voltage vs. K – partial view 33

LIST OF TABLES

Table 2-1. Theoretical predictions from previous MMIT[19,20,24] 14

Table 2-2. Latest MMIT operational parameters[27] 14

Table 4-1. Objective checklist of previous MMIT[23,24,27] 22

Table 4-2. Propellant and grid material of different thruster 26

Table 4-3. Threshold energy of different incident atom on target atom[6,40] 27

Table 4-4. Properties of different atoms 28

LIST OF SYMBOLS

A_{b}	=	Active beam area, m^2
A_{e}	=	Exhaust area of the nozzle, m^2
A_{c}	=	Cross-section area of a channel, m^2
A_{su}	=	Initial structural unit a hexagon area, m^2
D	=	Grid diameter, m
d_{h}	=	Hole diameter, m
e	=	Elementary charge, 1.6×10^{-19} C
F_{oaa}	=	Open area fraction
$(\mathrm{FP})_{\mathrm{a}}$	=	Impingement current density flatness parameter
$\vec{E}$	=	Electric field, J
E_{i}	=	Ion incident energy, eV
E_{th}	=	Threshold energy, eV
E_{ep}	=	Electric potential energy, J
E_{k}	=	Kinetic energy, J
g_{e}	=	Acceleration due to gravity at Earth's surface, 9.81 $m \cdot s^{-2}$
I_{b}	=	Ion beam current, A
I_{sp}	=	Specific impulse, s
j	=	Current density, A m^{-2}
j_{a}	=	Impingement current, A
j_{b}	=	Beam current, A
$J_{\mathrm{a,su}}$	=	Average ion impingement current in structural unit, A
J_{b}	=	Beam current density, $A \cdot m^{-2}$
J_{o}	=	Momentum out of the control volume, N
k_{e}	=	Lindhard electronic stopping coefficient
l_{cc}	=	Center-to-center hole spacing, m
l_{h}	=	Maximum distance of two adjacent holes, m
m	=	Atomic mass of ion, kg
m_{g}	=	Atomic mass of grid material, kg
m_{i}	=	Atomic mass of incident ion, kg
M_{i}	=	Initial mass of vehicle, kg

M_{f}	=	Final mass of vehicle, kg
M_{lo}	=	Mass loss of the structural unit, kg
M_{su}	=	Initial mass of the structural unit, kg
$\dot{m}$	=	Mass flow rate, kg·s^{-1}
$\dot{m}_{\mathrm{p}}$	=	Propellant mass flow rate, kg·s^{-1}
n	=	Number density, number·m^{-3}
N	=	Number of holes
U_{s}	=	Surface binding energy of the target solid, eV
P	=	Exhaust power, W
P_{a}	=	Ambient pressure, Pa
P_{e}	=	Exhaust pressure, Pa
P_{in}	=	Total input electrical power, W
P_{jet}	=	Jet power, W
q	=	Elementary charge, 1.6 × 10^{-19} C
r_{h}	=	Hole radius, m
S_{n}	=	Nuclear stopping cross section, Å·atom^{-1}
$s_{\mathrm{n}}^{\mathrm{TF}}$	=	Reduced nuclear stopping power from Tomas–Fermi potential
t	=	Thickness of grid, m
u_{e}	=	Exhaust velocity, m·s^{-1}
u_{eq}	=	Equivalent exhaust velocity, m·s^{-1}
Δu	=	Change in overall velocity, m·s^{-1}
V	=	Potential difference between grids, V
V_{a}	=	Potential difference between grids, V
w_{c}	=	Width of the channel, m
Y	=	Sputtering yield, atom·ion^{-1}
$Y_{\mathrm{net,Xe/Mo}}$	=	Average net sputtering yield of Xenon on Molybdenum, atom·ion^{-1}
γ	=	Energy transfer factor in the elastic collision
ϵ	=	Reduce energy, eV
ε_0	=	Vacuum permittivity, 8.854 × 10^{-12} F·m^{-1}
λ_{s}	=	Shape factor
λ_{y}	=	Stochastic factor

ρ_c	=	Charge density, $C \cdot m^{-3}$
ρ_g	=	Density of the grid material, $kg \cdot m^{-3}$
τ	=	Thrust, N
τ_L	=	Lifetime, s

ACKNOWLEDGMENTS

I am grateful to join this wonderful research group and to accomplish exciting work. This was a hard but a valuable time in my life. Thanks to my advisors Dr. Micci and Dr. Bilén who give me lots of space and time to experiment and to develop my research abilities. Thanks to Asif, my research partner, who has been the most helpful and talented friend. Amy Lu, my most honest friend who is always there and makes me a better person. Thanks to my friends back at home for all the support and understating during these crazy years. Special thanks to my mom Li-Fen Chou, my father Chien-Hsiung Hsieh, my silly sister Chien-Lin Hsieh, and my grandmom Shi Wu Chou, who support me and always encourage me to pursue my dreams.

Chapter 1

Introduction

Electric propulsion (EP) has become of significant interest for interplanetary exploration due to its higher efficiency and specific impulse than chemical propulsion. Among different types of electric thrusters, the gridded ion thruster is increasingly being used in space missions, with specific impulses usually on the order of thousands of seconds.

Ion thrusters typically produce very low thrust in comparison to chemical thrusters. However, they have a longer operational lifetime, which enables them to serve as in-space propulsion devices. In the early 1960s, Kaufman developed a functional prototype of an ion thruster at NASA Lewis (now NASA Glenn).[1] Later, in 1964, NASA launched the Space Electric Rocket Test (SERT-I), which conducted the first experimental testing of an electrostatic ion thruster in space, with an operational time of 31 minutes.[2] In the late 1990s, Deep Space 1 carried the NASA Solar Technology Application Readiness (NSTAR) engine as its primary source of propulsion, setting the stage for future ion-propelled spacecraft missions.[3] The 30,000-hour life test of the spare ion thruster from the Deep Space 1 mission has revealed several parameters that are to be considered in the development of ion thrusters.[4] One of these is grid lifetime.

1.1 Life Assessment

Grid erosion is one of the primary concerns that must be addressed for successful future missions. Moore et al., provided insight into the damage caused by exposure to the plasma discharge.[5,6] This damage was more severe than previously thought and mandated more research on thruster lifetime, as it impacts mission life and appropriate space system design. Since then there have been several research centers focusing on the grid life of ion thrusters, which serves as the platform for the research conducted in this thesis.[7–15]

1.2 Thesis Overview

This thesis presents progress on the assessment of grid life of the MMIT. Chapter 2 covers background information, previous research at Penn State, and relevant equations. Chapter 3 presents the equipment used in the latest experimental iteration and the measurement method. Chapter 4 provides the design criteria based on the results generated from the current version of the experimental data. Chapter 5 summarizes the research progress on the MMIT and provide potential changes to be implemented.

Chapter 2

Theoretical Background

This chapter covers the fundamentals of rocket propulsion leading to electric propulsion. The necessary physics of ion thrusters are also discussed here to understand the functionality of the MMIT. The last part covers the relevant equations to assess the life of the thruster.

2.1 Propulsion System

Any system that follows Newton's third law, which states that "for every action, there is a reaction with equal magnitude and opposite direction," to change vehicle's velocity, is called a propulsion system. Propulsion systems can be divided into several categories as shown in Figure 2-1, where our focus lies on understanding rocket propulsion. In chemical propulsion, the energy needed to generate thrust comes from breaking the chemical bonds and releasing energy, creating heat. Chemical propulsion is energy limited since only a limited amount of energy can be released from a chemical reaction. On the other hand, in electric propulsion, the propellants are usually accelerated by using electric and magnetic fields. Electric propulsion is power limited since there is only limited amount of electrical power on the spacecraft.

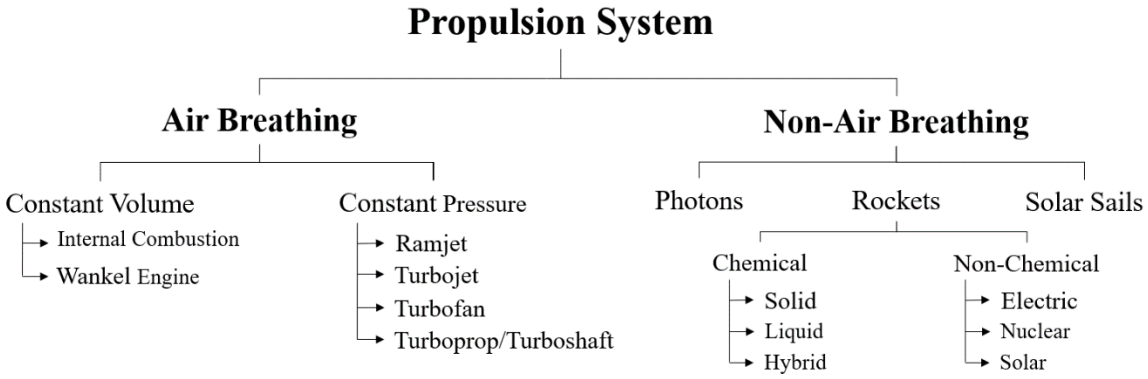

Figure 2-1. Categories of propulsion systems

2.2 Rocket Propulsion

To understand how a rocket works, let's take a look at the ideal rocket equation, or so called Tsiolkovsky rocket equation, which is derived from the conservation of momentum. The conservation of momentum for rocket engines can be illustrated using Figure 2-2, assuming that gravity is not acting on the control volume.[16] The ideal rocket equation expresses the change in vehicle velocity by using the change of mass ratio and exhaust velocity, which is written as

$$\Delta u = u_{\mathrm{e}} \ln \frac{M_{\mathrm{i}}}{M_{\mathrm{f}}}, \tag{2.1}$$

where u_{e} is exhaust velocity, M_{i} is the initial mass and M_{f} is the final mass.

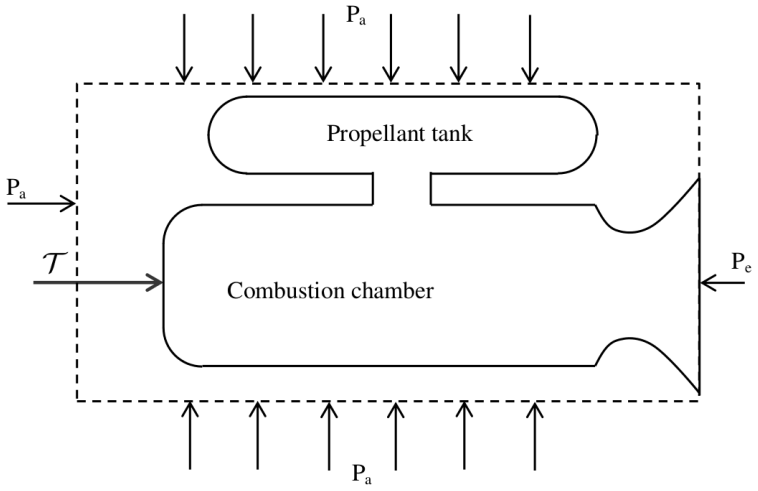

Figure 2-2. Forces acting on the control volume of a rocket engine[16]

Conservation of momentum states that momentum at the inlet of the control volume is equal to the momentum at the exit. In a rocket engine, there is no inflow of momentum. Hence the outflow momentum can be expressed as

$$J_{\mathrm{o}} = \dot{m} u_{\mathrm{e}}, \tag{2.2}$$

where $\dot{m}$ is the mass flow rate of exhaust and u_{e} is the exhaust velocity. The net force acting on the control volume of the rocket engine is equal to the change in momentum; therefore, the thrust can be expressed as

$$\tau = J_{\mathrm{o}} + (P_{\mathrm{e}} - P_{\mathrm{a}}) A_{\mathrm{e}} = \dot{m} u_{\mathrm{eq}}, \tag{2.3}$$

where P_e is the pressure at the exit, P_a is ambient pressure, and A_e is the area of exhaust. In Equation (2.3), we introduce a new term, u_{eq}, the equivalent exhaust velocity, which can be written as

$$u_{eq} = u_e + \frac{(P_e - P_a)}{\dot{m}} A_e \,. \tag{2.4}$$

To account for all the influences on the rocket engine as shown in Figure 2-2, we can rewrite Equation (2.1) into

$$\Delta u = u_{eq} \ln \frac{M_i}{M_f} \,. \tag{2.5}$$

Another important parameter is called the specific impulse. The specific impulse indicates the efficiency of propellant used by the rocket which can be written as

$$I_{sp} = \frac{\tau}{\dot{m} g_e} = \frac{u_{eq}}{g_e} \,. \tag{2.6}$$

2.3 Electric Propulsion

Electric propulsion generates thrust by accelerating the propellant using electrical or electromagnetic energy. With different methods to accelerate the propellant, electric propulsion can be categorized into one of three types: 1) Electrothermal: electric or electromagnetic energy is used to heat the propellant followed by nozzle expansion. Examples are resistojets that use electrical resistance heating and arcjets that use electrical arc heating. 2) Electrostatic: a steady electric field is used to accelerate an ionized propellant. Examples are ion thrusters, hall thrusters, and field emitters. 3) Electromagnetic: a combination of electric and magnetic fields, steady or unsteady, is used to accelerate an ionized propellant. Examples are magnetoplasmadynamic thrusters, pulsed plasma thrusters, and pulsed inductive thrusters.

2.3.1 Ion Thruster

The operation of ion thrusters can be divided into three primary processes: ionization, acceleration, and neutralization. First, neutral propellant is ionized. Second, the static electric field

accelerates and expels ions to generate thrust. Finally, in order to prevent beam stalling, the thruster exhaust needs to be neutralized. Figure 2-3 shows the schematic of an ion thruster.

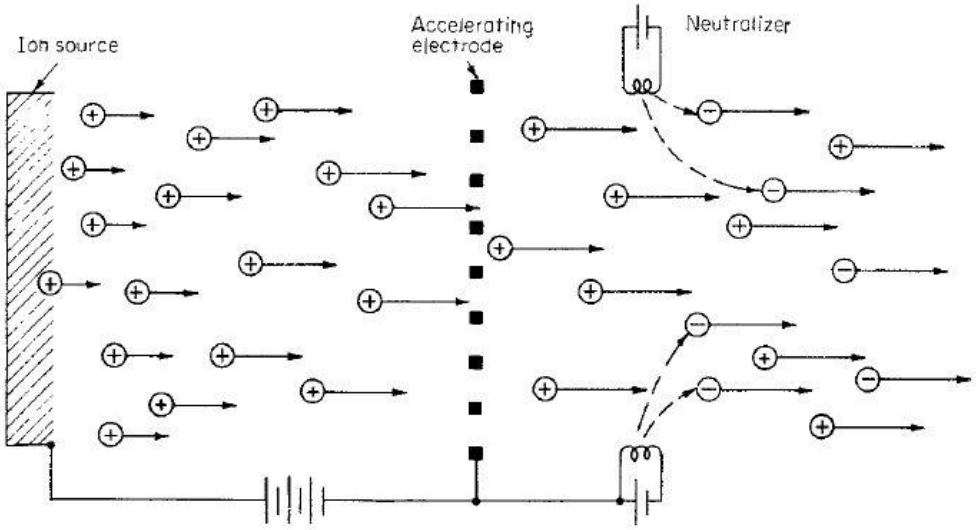

Figure 2-3. Schematic of ion thruster[2]

2.3.1.1 Ionization

Ionization is the process that ionizes the propellant and there are several processes that can accomplish this. We discuss three types of ionization: electron bombardment ionization, radio-frequency ionization, and microwave frequency ionization with electron cyclotron resonance.

- Electron Bombardment Ionization

In 1961, Kaufman developed a thruster that used a cathode to emit electrons, with the discharge chamber severing as the anode. The electric field created by the anode and cathode and a magnetic field resulting from an external coil or permanent magnets controls the electron motion. These electrons collide with neutral atoms and then the neutral atoms will be split into ions and electrons. Figure 2-4 shows the schematic of a Kaufman thruster.

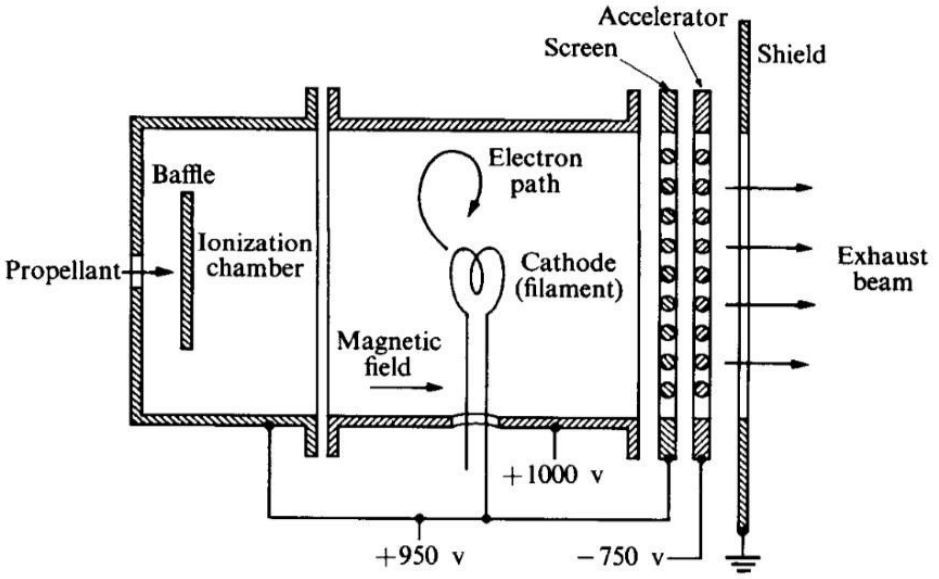

Figure 2-4. Schematic of Kaufman thruster[16]

- Radio-Frequency Ionization

Different than the Kaufman thruster, radio-frequency thrusters do not contain a cathode and anode. The induced electric field that results from RF coils surrounding the discharge chamber provides energy to free electron, and these energetic electrons cause ionization. Figure 2-5 shows a schematic of a radio-frequency ion thruster.

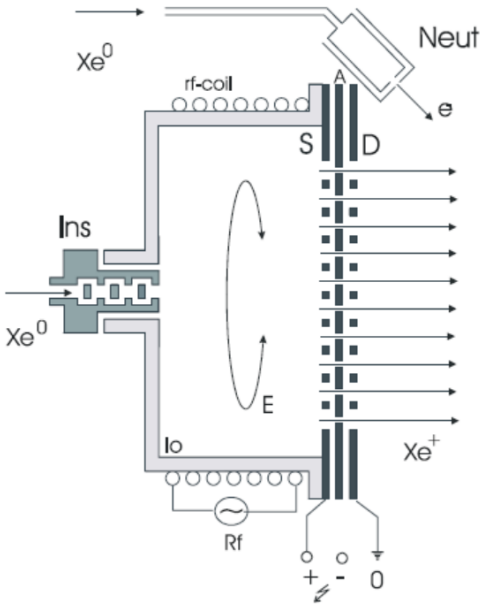

Figure 2-5. Schematic of radio-frequency ion thruster[17]

- Microwave-Frequency Ionization with Electron Cyclotron Resonance

The microwave-frequency ion thruster contains an antenna and permanent magnets. The ionization process results from the interaction between an electromagnetic wave transferred through an antenna and a strong magnetic field created by permanent magnets. Electron cyclotron resonance (ECR) is generated from the interaction between the electromagnetic wave and the magnetic field. The ECR region confines and provides energy to the electrons. The energetic electrons collide with neutral atoms to ionize them.

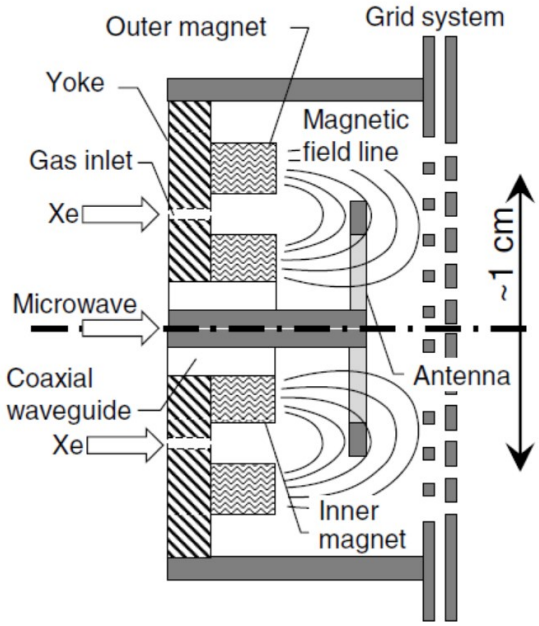

Figure 2-6. Schematic of Microwave-frequency ion thruster[18]

2.3.1.2 Acceleration

Ion thrusters use grids to accelerate the ions and generate thrust. According to Newton's third law, the more mass the system expels, the more force generated acting on the system in the opposite direction. Ion thrusters function by extracting ions out of the thruster instead of electrons because ions are heavier than electrons. For two-grid systems, one is the screen grid and the other is the acceleration grid. The screen grid is biased positively and the acceleration grid is biased negatively. The potential difference causes the electric field to extract the ions. The reason for the

negative acceleration grid bias is to keep electrons in the discharge chamber and prevent the downstream electrons from back streaming.

The force in the accelerating section is provided from the electric field between two grids. According to the conservation of energy, the electric potential energy is equal to the kinetic energy of the charged particle, which can be written as

$$E_{\mathrm{ep}} = qV\ , \tag{2.7}$$

$$E_{\mathrm{k}} = m\frac{{u_{\mathrm{e}}}^2}{2}\ , \tag{2.8}$$

where E_{ep} is the electric potential energy, q is the elementary charge, V is the voltage difference between the two grids, E_k is the kinetic energy, m is the ion mass, and u_{e} is the exhaust velocity. The exhaust velocity can be written as

$$u_{\mathrm{e}} = \sqrt{\frac{2qV}{m}}\ . \tag{2.9}$$

Thrust can be written in terms of the electric potential and beam current. Mass flow rate can be written in terms of beam current, which can be written as

$$\dot{m} = \frac{I_{\mathrm{b}}m}{q}\ , \tag{2.10}$$

where $\dot{m}$ is mass flow rate and I_{b} is beam current. From Equation (2.3), thrust can be written as

$$\tau = \frac{I_{\mathrm{b}}m}{q}\cdot\sqrt{\frac{2qV}{m}} = I_{\mathrm{b}}\sqrt{\frac{2mV}{q}}\ . \tag{2.11}$$

Exhaust power can be written as

$$P = I_{\mathrm{b}}V = \dot{m}\frac{u_{\mathrm{e}}^2}{2}\ . \tag{2.12}$$

From Equation (2.12), increasing mass flow rate can increase the beam current. The higher beam current will increase thrust. However, there exists a limitation in mass flow rate called the space charge effect. The accumulative charges between the grids will locally form an electric field and further change the potential profiles between electrodes. Figure 2-7 shows the space charge effect.

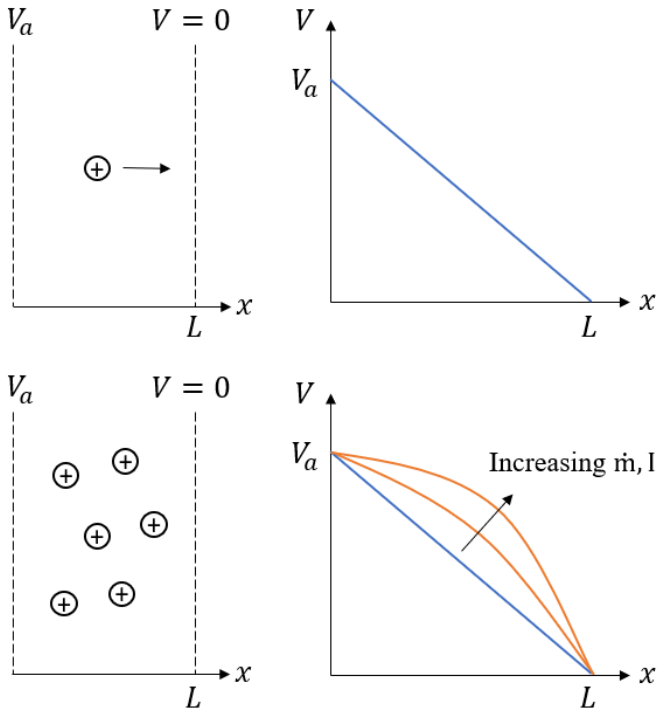

Figure 2-7. Space-charge effect

To calculate the space-charge-limited current one starts with one of Maxwell's laws

$$\nabla \cdot \vec{E} = \frac{\rho_c}{\varepsilon_0}, \tag{2.13}$$

where $\vec{E}$ is the electric field, ρ_c is the charge density and ε_0 is the vacuum permittivity. Equation (2.13) can be written as

$$\nabla^2 V = -\frac{\rho_c}{\varepsilon_0}. \tag{2.14}$$

In one dimension, the above equation can be written as

$$\frac{d^2V}{dx^2} = -\frac{nq}{\varepsilon_0} = -\frac{j}{\varepsilon_0 u_e} = \frac{-j}{\varepsilon_0\sqrt{2q/m}}(V_a - V)^{-1/2}, \tag{2.15}$$

where n is the ion number density, j is the current density, and u_e is the exhaust velocity. Integrating Equation (2.15), one gets the potential as a function of position,

$$V(x) = V_a - \left[\frac{3}{2}\sqrt{\frac{j}{\varepsilon_0}}\left(\frac{m}{2q}\right)^{\frac{1}{4}} x\right]^{\frac{4}{3}}. \tag{2.16}$$

Since $V = 0$ at $x = L$, where L is the grid separation, the current density given by Child's Law can be written as

$$j = \frac{4\varepsilon_0}{9}\sqrt{\frac{2q}{m}}\frac{V_a^{3/2}}{L^2}. \tag{2.17}$$

Thrust density can be express as thrust per beam area, which can be written as

$$\frac{\tau}{A} = \frac{\dot{m}u_e}{A} = \frac{8}{9}\varepsilon_0\left(\frac{V_a}{L}\right)^2. \tag{2.18}$$

2.3.1.3 Neutralization

When operating the ion thruster, it continuously expels positively charged ions, which means the spacecraft will accumulate negative charge and bias negatively. In contrast, the surrounding region will have plenty of ions, which means that region is biased positively. Therefore, the thruster will attract back the emitted ions which it just expelled, resulting in zero thrust. This phenomenon is called beam stalling. In order to prevent beam stalling, a neutralizer is necessary in an ion thruster. There are many different methods to generate electrons, for example: thermionic emitters, electron gun, and field emission.

2.4 Previous Research in Penn State

The Pennsylvania State University has been developing miniature electric propulsion devices for several decades. The first version of a miniature ion thruster was developed by Trudel[19] as a Miniature Radio-Frequency Ion Thruster (MRIT) and later studied by Mistoco.[20] The 1-cm MRIT (Figure 2-8) operated at 16 W of input power and 0.038 sccm of argon.

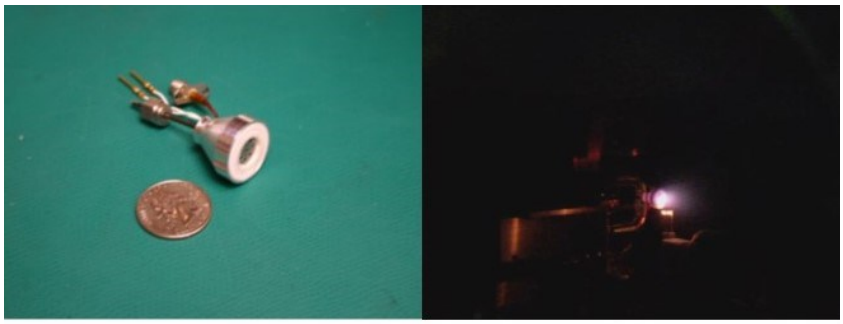

(a) (b)

Figure 2-8. Trudel's MRIT (a) compared to a U.S. quarter (b) operational test in a vacuum chamber[19]

Lubey redirected the focus towards microwave-frequency thrusters, inspired by JAXA's μ1 engine,[21] which utilized ECR for generating plasma. This design of the Miniature Microwave-Frequency Ion Thruster (MMIT) incorporated design parameters from the MRIT, which caused performance issues. Lubey's MMIT was not successful in efficient plasma generation but served as a platform for the future MMIT designs. Based on Equation (2.11), his thruster had a theoretical predicted thrust of 258 μN with running at 1 W of input power using xenon as the propellant.[22,23] Figure 2-9 shows Lubey's MMIT operating in vacuum conditions in the research facility at Penn State.

Figure 2-9. Lubey's MMIT operational test in a vacuum chamber[23]

Taunay redesigned the MMIT with major changes based more on the μ1 design as seen in Figure 2-10 and performed several numerical analyses to understand the ECR plasma generation process. Taunay's MMIT was successful in plasma generation but could not sustain it long enough

to extract an ion beam. His theoretical prediction for thrust was 217 μN at 8 W of input power using argon as the propellant.[24,25] Figure 2-11 shows Taunay's MMIT operating in vacuum conditions with the two sets of grids developed for testing. Table 2-1 shows the theoretical predictions made for the MRIT and MMIT.

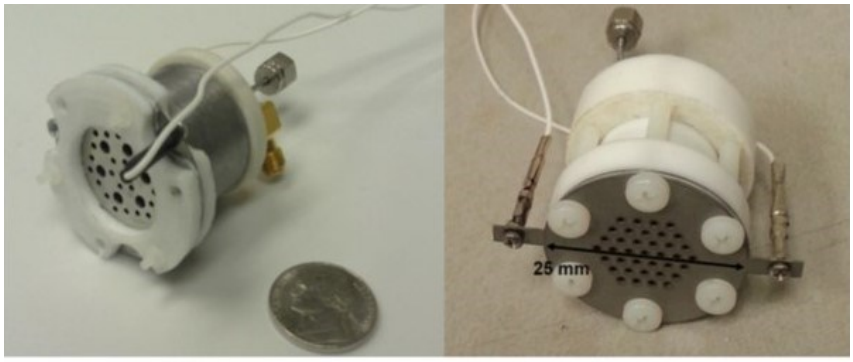

Figure 2-10. (a) Lubey's MMIT[23], (b) Taunay's MMIT[24]

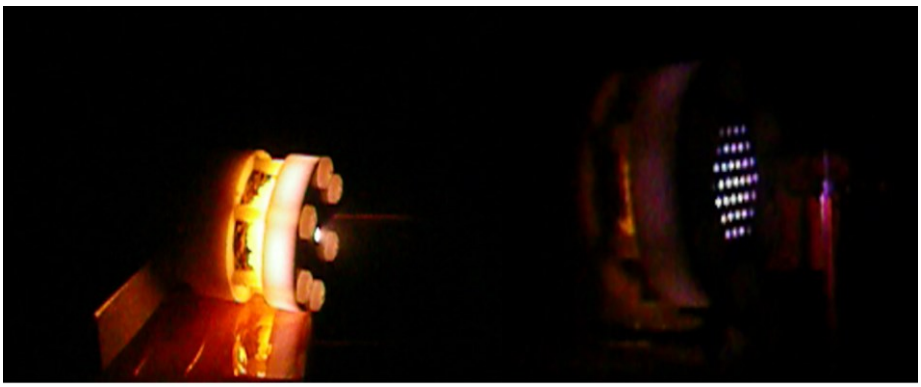

Figure 2-11. Taunay's MMIT operational test in a vacuum chamber, (a) single-hole grid configuration, and (b) extraction grid configuration.[24]

Table 2-1. Theoretical predictions from previous MMIT[19,20,24]

Parameter	MRIT	MMIT
Propellant	Argon	Argon
Thrust	64.8 μN	217 μN
Specific impulse	2462 s	10,700 s
Input power	16 W	8 W
Input frequency	1.5 MHz	5 GHz
Mass flow rate	0.038 sccm	0.25 sccm
Propellant utilization efficiency	41.1%	46%

2.5 Latest MMIT Research

Research at Penn State has been an iterative process between numerical simulations and experimental research. The latest prototype of the MMIT was an extension of Taunay's design, which was optimized by Asif to successfully extract the ion beam and produce thrust. Asif's MMIT (Figure 2-12) had an improved efficiency and was able to generate plasma at 2.6 W of power using 0.25 sccm of argon and could sustain plasma at powers as low as 0.1 W.[26] This version of the MMIT had a calculated thrust of 0.01 mN and specific impulse of 2470 s.[27] Table 2-2 shows the latest MMIT operational parameters. Figure 2-13 shows the MMIT operating under different accelerating voltages.

Table 2-2. Latest MMIT operational parameters[27]

Parameter	MMIT
Propellant	Argon
Thrust	100 μN
Specific impulse	2470 s
Input frequency	4.98 GHz
Mass flow rate	0.25 sccm

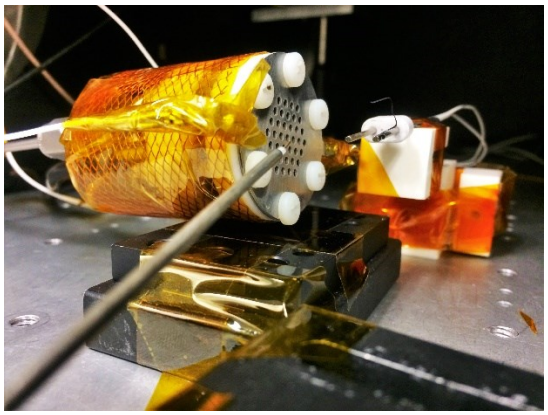

Figure 2-12. Asif's MMIT[26]

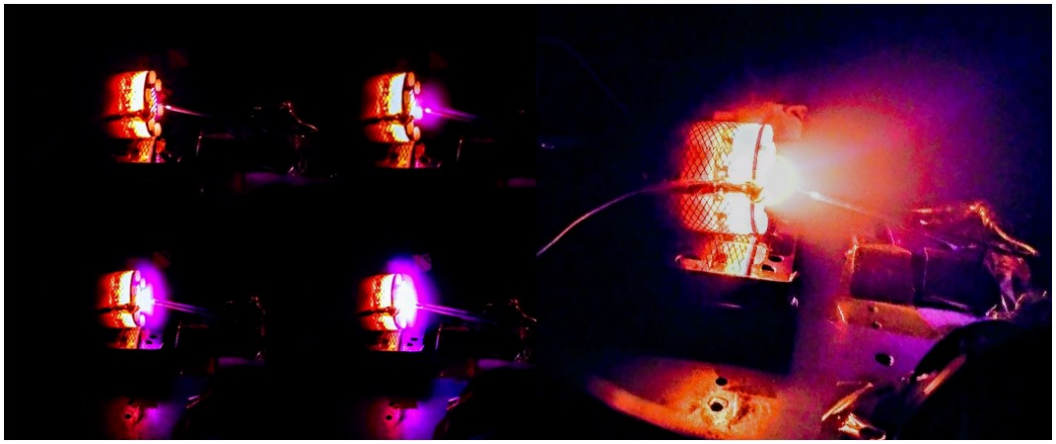

Figure 2-13. Asif's MMIT operating with different accelerating voltages[26]

2.6 Grid Erosion

Since the early 1990s, NASA and JPL have published several papers concerning life prediction.[6,28,29] Polk showed the fundamental calculation of a grid's life.[6] Many processes cause grid erosion. NASA, JPL, and JAXA mainly discussed charge exchange collisions and the impingement of ions.[6,30,7,31,32] Grid erosion is caused mainly by ion impingement. Those impinging ions result from the neutral atoms in between the grids and downstream of the grids. In an ion thruster, the ions are accelerated by an axial electric field created by the two grids. The acceleration grid is biased negatively to prevent electrons from the neutralizer from back streaming into the discharge chamber. The acceleration grid collects slow ions generated from charge exchange collisions with neutral atoms in between the grids and downstream of the grid.

Neutral gas leaks from the ionization chamber and when ionized generates ions downstream and between the grids. In space, the thruster is the only source of neutral gas; therefore, only the propellants from the thruster will cause erosion. On the other hand, in ground tests, not just the propellant from the thruster but also the experimental facility could contain neutral gas. The neutral gas can be ionized in two ways: collision with the electrons from the neutralizer and charge-exchange collisions. The ionization process of the neutral gas is dominated by the charge-exchange collision. The electron collisions have a relatively small effect on the ionization process. A charge-exchange collision is a process in which energetic ions interact with neutral atoms and carry away the electron in the neutral atom. The fast ion rebinds with the stolen electron and becomes an energetic neutral atom. The results of this process are slow ions and fast neutral atoms. Figure 2-14 shows the charge-exchange process.

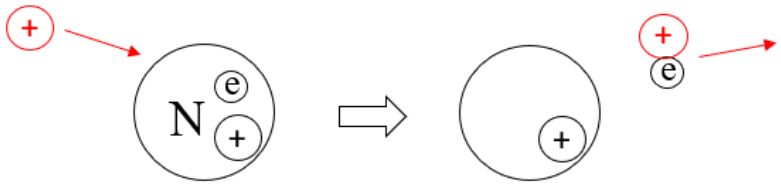

Figure 2-14. Charge-exchange collision

The slow ions from the charge-exchange collision are mainly created downstream of the acceleration grid. That type of ion will cause grid erosion since those ions do not have enough energy to escape the potential attraction form the acceleration grid and are drawn back to the outer surface of the acceleration grid. This phenomenon leads to a potential drop near the acceleration grid in the gap and downstream. Therefore, those ions in the downstream neutralization area will be attracted back toward the grid.

2.7 Life Assessment Calculation of Grids

Unlike NASA and JAXA's case, the main cause of grid erosion in the MMIT is not impingement ions. The two main reasons causing damage to the MMIT grids are grid arcing and sputtering yield. The arcing issue is mainly caused by the sharp edges on the grids, which is partially due to manufacturing issues that can be partially addressed. As the deformation of the hole diameter occurs during erosion, the uneven shapes of the holes will increase the susceptibility to arcing.

Sputtering occurs when the ion energy overcomes the binding energy on the surface of the grid material. The geometry of the grid will change as the grid material erodes/sputters away and can eventually cause complete structural failure due to loss of strength of the grid. Also, the worn-out grid will lose ion optic focusing capability, which means it can no longer accelerate the ions or prevent the electrons from back streaming.

The prediction of the grid life depends on the mass loss rate of the grids. The deformation of the grids plays an important role in the mass equation.[6,33] We defined the failure criterion to be when mass loss is equal to mass loss allowed, which can be written as

$$\left(\frac{M_{\mathrm{lo}}}{M_{\mathrm{su}}}\right) = \left(\frac{M_{\mathrm{lo}}}{M_{\mathrm{su}}}\right)_{\mathrm{a}}, \tag{2.19}$$

where the mass loss of the grid can be written as

$$\left(\frac{M_{\mathrm{lo}}}{M_{\mathrm{su}}}\right) = \frac{J_{\mathrm{a,su}}\tau_L Y_{\mathrm{net}} m_{\mathrm{g}}}{eM_{\mathrm{su}}}, \tag{2.20}$$

where M_{lo} represents the mass loss of the structural unit, M_{su} is the initial mass of the structural unit, τ_L is the operating time, $J_{\mathrm{a,su}}$ is average ion impingement current in the structural unit, Y_{net} is the average net sputtering yield, m_{g} is mass per atom of grid material, and e is the elementary charge. The average ion impingement current in the structural unit can be written as

$$J_{\mathrm{a,su}} = \left(\frac{J_{\mathrm{a}}}{J_{\mathrm{b}}}\right)\frac{J_{\mathrm{b}}\, A_{\mathrm{su}}}{A_{\mathrm{b}}(1-F_{\mathrm{oaa}})(\mathrm{FP})_{\mathrm{a}}} \tag{2.21}$$

where A_{su} is the initial structural unit hexagonal area, A_{b} is the active beam area, F_{oaa} is the open area fraction, $J_{\mathrm{a}}/J_{\mathrm{b}}$ is the ratio of impingement current to beam current and $(\mathrm{FP})_{\mathrm{a}}$ is the impingement current density flatness parameter. The initial structural unit is a hexagonal area that can be calculated from

$$A_{\mathrm{su}} = \frac{\sqrt{3}}{12} l_{\mathrm{cc}}^2 - \pi\frac{d_{\mathrm{h}}^2}{24}, \tag{2.22}$$

where l_{cc} is the center-to-center hole spacing, and d_{h} is the hole diameter. The flatness parameter represents the macroscopic nonuniformity in the mass loss distribution across the grid. The active beam area and open area fraction can be written as

$$A_{\mathrm{b}} = N\frac{\pi d_{\mathrm{h}}^2}{4}, \tag{2.23}$$

$$F_{\mathrm{oaa}} = \frac{Nd_{\mathrm{h}}^2}{D^2 - Nd_{\mathrm{h}}^2}, \tag{2.24}$$

where N is the number of holes in the grid and D is the grid diameter. The initial mass of the structural unit M_{su} can be calculated from

$$M_{\mathrm{su}} = \rho_{\mathrm{g}} A_{\mathrm{su}} t, \tag{2.25}$$

where ρ_{g} is the density of the grid material, and t is the thickness of the grid. The average net sputtering yield Y_{net} for xenon on molybdenum can be predicted from[34]

$$Y_{\mathrm{net,Xe/Mo}} = \lambda_y a {E_{\mathrm{i}}}^b \left(1 - \frac{E_{\mathrm{th}}}{E_{\mathrm{i}}}\right)^c \left(1 + \frac{m_{\mathrm{i}} E_{\mathrm{th}}}{E_{\mathrm{i}}}\right)^d , \tag{2.26}$$

where λ_y is the stochastic factor representing variations of average net yield from the yield at normal incidence, E_{i} is the ion incident energy, E_{th} is the threshold energy for sputtering, and m_{i} is the atomic mass of the incident ion. The parameters a, b, c, and d are the estimated values from experimental data.[34,35] The ion incident energy E_{i} is given by

$$E_{\mathrm{i}} = eV_{\mathrm{a}} , \tag{2.27}$$

where V_{a} is the potential difference between the two grids. The mass allowed is defined as when the first structural unit is divided into two, which can be written as

$$\left(\frac{M_{\mathrm{lo}}}{M_{\mathrm{su}}}\right)_{\mathrm{a}} = \frac{L_{\mathrm{c}} A_{\mathrm{c}}}{t A_{\mathrm{su}}} , \tag{2.28}$$

where A_{c} is cross-sectional area of a channel and L_{c} is the effective channel length, which can be written as

$$L_{\mathrm{c}} = \frac{\sqrt{3}}{6} l_{\mathrm{cc}} . \tag{2.29}$$

The cross-section area of a channel A_{c} can be written as

$$A_{\mathrm{c}} = \frac{2}{3} \lambda_{\mathrm{s}} w_{\mathrm{c}} t , \tag{2.30}$$

where λ_{s} is the shape factor, w_c is the width of the channel and t is the thickness of the grid. From Equation (2.19) and Equation (2.28), failure criterion can be written as

$$\frac{J_{\mathrm{a,su}} \tau_L Y_{\mathrm{net}} m_{\mathrm{g}}}{e M_{\mathrm{su}}} = \frac{L_{\mathrm{c}} A_{\mathrm{c}}}{t A_{\mathrm{su}}} . \tag{2.31}$$

Therefore, the life equation of the grids τ_L can be expressed as

$$\tau_L = \frac{L_{\mathrm{c}} A_{\mathrm{c}} e M_{\mathrm{su}}}{t A_{\mathrm{su}} J_{\mathrm{a,su}} Y_{\mathrm{net}} m_{\mathrm{g}}} . \tag{2.32}$$

Chapter 3

Experimental Setup and Measurement Method

This section presents the experimental setup for testing the MMIT. The experimental results acquired from the latest version of the MMIT were used in this thesis to determine an approximation for the life of the thruster.[27] The experimental work on the MMIT is not part of the thesis but overviewed herein for situating and motivating the current work.

3.1 Vacuum Chamber System

The experiments were conducted in a thermal vacuum chamber in a research facility located at Penn State. The vacuum chamber is a 0.6-m-radius × 1.0-m-length cylinder.[29] High vacuum conditions are reached using a dual pump system using a BOC Edwards IPUP dry pump and a CTI-Cryogenics Cryo-Torr 10 series cryopump shown in Figure 3-1.

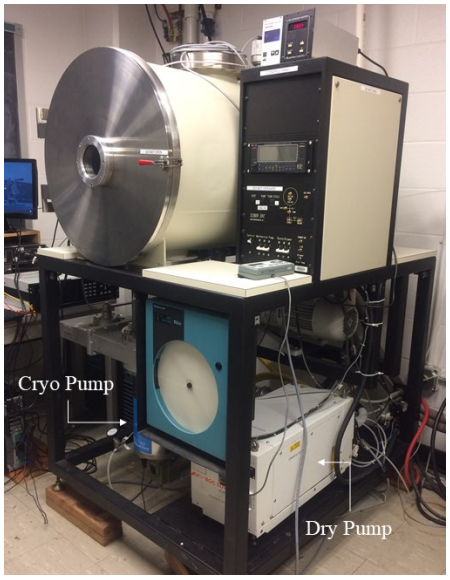

Figure 3-1. Vacuum chamber and pumps

3.2 MMIT System

The MMIT consists of three main systems that are operated during the experimental procedures: microwave system, propellant system, and extraction system. This excludes the other systems used to monitor and regulate the experimental conditions. A Keithley 2410 source meter coupled with a Langmuir probe and Faraday cage were used to make the measurements of the ion beam. Figure 3-2 shows an overview of the test setup.

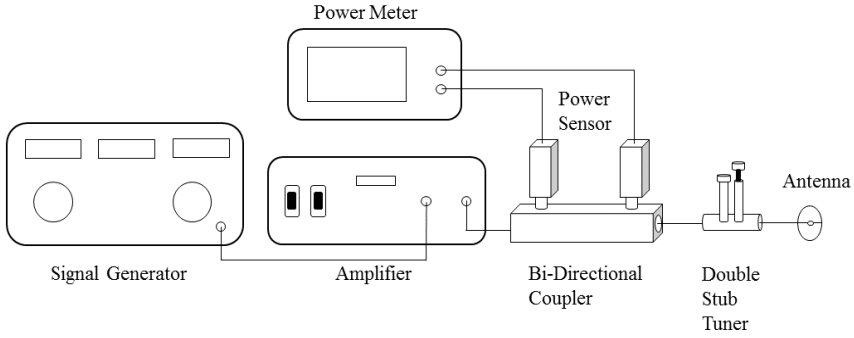

Figure 3-2. Schematic for microwave power injection into MMIT[26]

3.3 Propellant and Extraction System

The propellant system consists of an MKS Multi Gas Controller 647B, which controls the MKS ALTA Digital Mass Flow Controller 1480A. The 647B is preset with the necessary conditions to regulate the mass flow coming from a tank of 99.999% purity argon. The tank is fitted with standard regulators used to control the pressure of the gas. A Swagelok fitting is used along with a stainless-steel pipe to act as the gas feed through line to the thruster. The extraction grid voltage is supplied using a Stanford Research Systems, Inc. Model PS310 high voltage power supply with a max DC voltage rating of 1250 V[36] and an Oriel 70705 high-voltage power supply with a max DC voltage rating of 2000 V.[37] A BNC-connector cable is used to transmit the high voltage supply.

3.4 Measurement Method

A digital Vernier caliper was used to measure the dimensions of the grid. The range of the caliper is 0 to 150 mm and the accuracy is 0.02 mm with resolution of 0.01 mm.[38] To determine what damage may have occurred to the grid, it was measured before and after operation. For the hole diameter, the measurement method is straight forward. For hole spacing, we first measure each hole diameter and then measure each distance with adjacent holes as shown in Figure 3-4. The equation for each adjacent spacing can be expressed as

$$l_{\mathrm{cc}_1} = l_{\mathrm{h}_1} - (r_{\mathrm{h}_1} + r_{\mathrm{h}_3}) , \tag{3.1}$$

$$l_{\mathrm{cc}_2} = l_{\mathrm{h}_2} - (r_{\mathrm{h}_1} + r_{\mathrm{h}_2}) , \tag{3.2}$$

$$l_{\mathrm{cc}_3} = l_{\mathrm{h}_3} - (r_{\mathrm{h}_2} + r_{\mathrm{h}_3}) , \tag{3.3}$$

where l_{h} is the maximum distance of two adjacent holes and r_{h} is the hole radius. The above equations are applicable for each adjacent hole spacing.

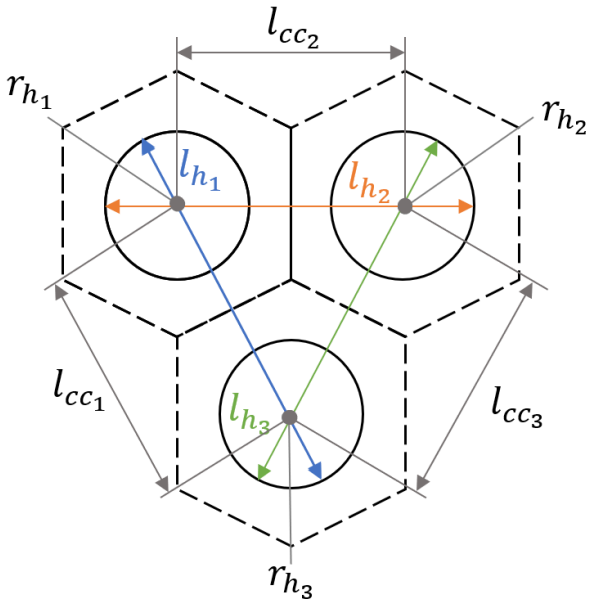

Figure 3-4. Schematic of measurement

Chapter 4

MMIT Design Criteria

The research thrust of this thesis is to establish better design criteria for the next prototype of the MMIT. This chapter provides an overview of previous iterations of the thruster and their respective design guidelines. Understanding the results from the grid life of the latest MMIT has shown significant gaps in the previous iterations that are crucial in achieving a fully functional flight version of the thruster.

4.1 Previous Design

Our objective for the MMIT prototype can be separated into three parts: plasma generation, plasma sustainment, and ion extraction. As mentioned above, development is an iterative process. Each iteration will take the previous lessons learned into account and fold them into a new prototype. The first prototype was developed by Lubey. He focused on plasma generation.[23] The second prototype was developed by Taunay. In Taunay's iteration, he focused on using numerical simulations to verify the position of the antenna and different geometries of the permanent magnets and yoke plate.[24] The final prototype was developed by Asif. He successfully extracted ions and sustained the plasma with lower power based on the modification of the resonant frequency and prevention of arcing.[27] Table 4-1 shows the objective check list of different versions of the MMIT. After the last design iteration, the MMIT research at Penn State has resulted in a functional prototype.

Table 4-1. Objective checklist of previous MMIT[23,24,27]

Thruster	Plasma Generation	Sustain Plasma	Ion Extraction
Lubey	✓	×	×
Taunay	✓	×	×
Asif	✓	✓	✓

Significant improvements suggested in the previous iterations were:

- Impedance matching: Impedance matching can maximize the power transfer.

- Faraday cage: A Faraday cage around the discharge chamber can reduce the external interference and contain fields within the discharge chamber.
- Better manufacturing: To prevent the arcing problem, micromachining and good design can help to keep the sharp edges.

4.2 Latest Design Overview of MMIT

The MMIT's operation can be divided into three main processes, each represented by a section of the thruster: initialization, ionization, and extraction. The initialization section represents pre-ionization processes such as the propellant inlet and installation of the antenna. The ionization section represents the components for ionization such as the yoke plate, permanent magnets, and antenna. The extraction section is composed of the grids used for accelerating the ions to generate thrust

In order to assemble each component, the thruster contains three main plates: back plate, yoke plate, and grid plate. The back plate supports the components in the initialization section. The yoke plate supports the components in the ionization section. The grid plate supports components in the extraction section. The back plate and the grid plate are made of MACOR, which has high thermal insulation and very low outgassing. The yoke plate is made of low carbon steel, which has a high permeability.

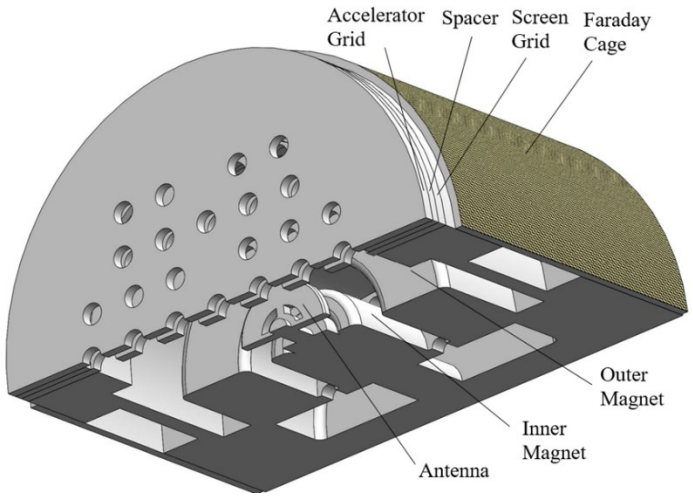

Figure 4-1. Cross-section view of latest MMIT prototype[27]

4.3 Calculation of Grid Life

In the latest version of the MMIT, the grids were damaged by arcing and sputtering.[27] To account for the damage in the thruster, we refer to Polk's equation,[6] which calculates the impingement damage of the grids. For Polk's grids, the impingement damage caused the formation of grooves and pits. However, the damage on the MMIT was due to arcing and sputtering. The damage of the MMIT caused the deformation of the grids. Therefore, we redefine the meaning of the parameters in Polk's equation to address the difference between the two cases.

As shown in Figure 4-2, the grids of MMIT have a hexagonal pattern of holes with each one surrounded by a hexagon, which we define as a structural unit.

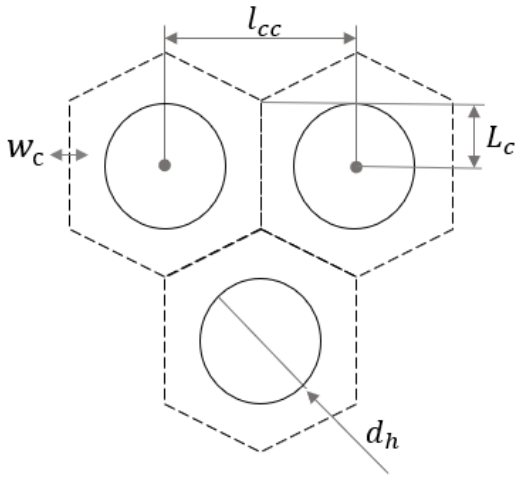

Figure 4-2. Structural unit of MMIT

In Chapter 2, we presented the basic derivation of the life equation from Equation (2.19) to Equation (2.32). There are two types of the variables in Equation (2.32), certainties and uncertainties. Some of the parameters in Equation (2.32) change from time to time and under different operating conditions, hence, there does not exist a fixed value. We defined those parameters that cannot be well defined as uncertainties: shape factor λ_s, flatness parameter$(\mathrm{FP})_\mathrm{a}$ and impingement current J_a. The certainties are the variables that can be measured or calculated: the hole diameter d_h, the center-to-center hole spacing l_cc, and the voltage difference V_a. We defined a new parameter K, which represents the certainties in the life equation, which can be written as

$$K = \frac{L_\mathrm{c} e M_\mathrm{su}}{t A_\mathrm{su} Y_\mathrm{net} m_\mathrm{g}}. \tag{4.1}$$

Hence, the life equation can be rewritten as

$$\tau_L = K \frac{A_c}{J_{a,su}}. \tag{4.2}$$

4.4 Experimental Findings

We target the fundamental variables in the K equation: the hole diameter, the center-to-center hole spacing, and the voltage difference. First, we target the hole diameter d_h and center-to-center hole spacing l_{cc}. The dimension and position of the hole will not be the same for each one because of deviation during the manufacturing process. The expected value of the hole diameter is 1.3208mm and center-to-center hole diameter is 3 mm. We assumed the average of the measurements as the initial value. The initial hole diameter measured is 1.321 mm and initial center-to-center hole spacing is 3.004 mm.

Figures 4-3 and 4-4 show the measurement of the grid after the thruster was operated for a period of time. The hole diameter after operating expanded as shown in Figure 4-3. From Equations (3.1) to (3.3), each hole spacing can be calculated as shown in Figure 4-4. The hole spacing does not increase for all of the holes. This uneven deformation results from the uneven geometry of the grid holes and also the recombination of the ions.

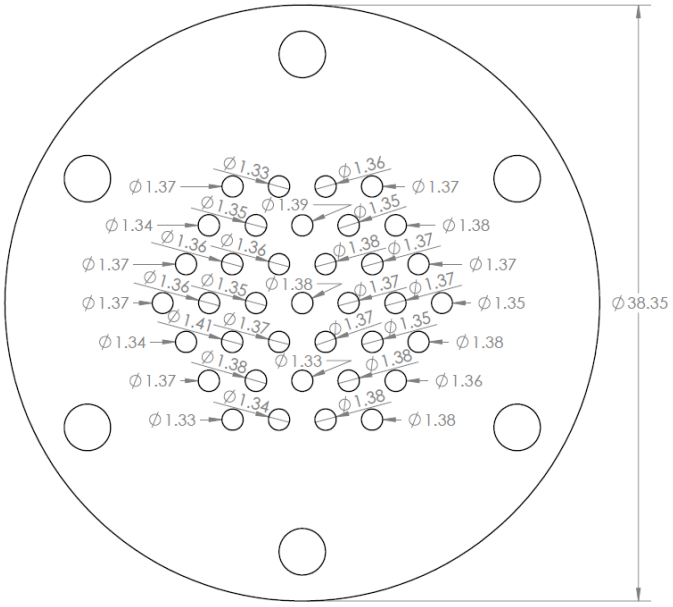

Figure 4-3. Hole diameter after operating

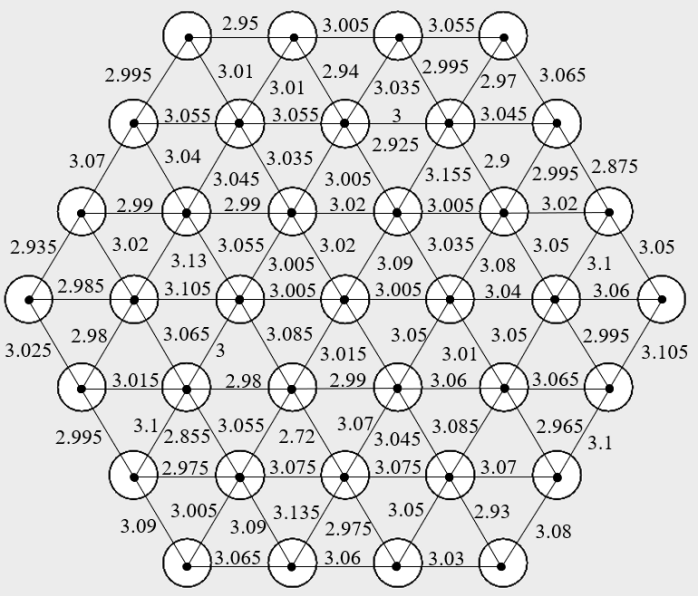

Figure 4-4. Center-to-center hole spacing after operating

In Table 4-2, the different operation conditions of each thruster are presented. The K value was extended to different thrusters to see the difference. The flight thruster stands for the current geometry of the MMIT with xenon as the propellant and molybdenum as the grid material. The experimental voltage differences varies from 300 V to 2000 V.

Table 4-2. Propellant and grid material of different thruster

Thruster	**Propellant**	**Grid Material**
JPL	xenon	molybdenum
Latest	argon	stainless steel
Flight	xenon	molybdenum

The sputtering yield presented in Chapter 2 is for xenon on molybdenum. In the latest prototype of the thruster, we use argon on stainless steel. To make the prediction more accurate, we apply another equation for calculating the sputtering of argon on stainless steel,[39] which can be written as

$$Y = 0.042 \frac{Q\,\alpha^*}{U_\mathrm{s}} \frac{S_\mathrm{n}(E_\mathrm{i})}{1 + \Gamma\, k_\mathrm{e}\, \epsilon^{0.3}} \left[1 - \sqrt{\frac{E_\mathrm{th}}{E_\mathrm{i}}}\right]^s , \tag{4.3}$$

where Q and s are the fitting parameters that can be found in Yamamura and Tawara's paper.[39] E_th is the sputtering threshold, which can be calculated from

$$\frac{E_\mathrm{th}}{U_\mathrm{s}} = \frac{1 + 5.7\,(M_1/M_2)}{\gamma}, M_1 \leq M_2 ,$$

$$= \frac{6.7}{\gamma}, M_1 \geq M_2, \tag{4.4}$$

where γ is the energy transfer factor in the elastic collision given by

$$\gamma = \frac{4\, M_1 M_2}{(M_1+M_2)^2}, \tag{4.5}$$

where M_1 and M_2 are the atomic masses of the incident and target atoms and α^* is the fitting parameter as a function of the mass ratio M_2/M_1, which can be calculated from

$$\begin{aligned} \alpha^* &= 0.249(M_2/M_1)^{0.56} + 0.0035(M_2/M_1)^{1.5}, M_1 \leq M_2, \\ &= 0.0875(M_2/M_1)^{-0.15} + 0.165(M_2/M_1), M_1 \geq M_2, \end{aligned} \tag{4.6}$$

U_s is the surface binding energy of the target solid, which can be found in Yamamura and Tawara's paper.[39] $S_{\mathrm{n}}(E_{\mathrm{i}})$ is the nuclear stopping cross section, which can be calculated from

$$S_{\mathrm{n}}(E_{\mathrm{i}}) = \frac{84.78\, Z_1\, Z_2}{({Z_1}^{2/3} + {Z_2}^{2/3})^{1/2}} \frac{M_1}{M_1 + M_2} s_{\mathrm{n}}^{\mathrm{TF}}(\epsilon), \tag{4.7}$$

where Z_1 and Z_2 are the atomic numbers of the incident and target atoms and $s_n^{\mathrm{TF}}(\epsilon)$ is the reduced nuclear stopping power from Tomas–Fermi potential:[40]

$$s_{\mathrm{n}}^{\mathrm{TF}}(\epsilon) = \frac{3.441\sqrt{\epsilon}\ln(\epsilon + 2.718)}{1 + 6.355\sqrt{\epsilon} + \epsilon(6.882\sqrt{\epsilon} - 1.708)}, \tag{4.8}$$

where ϵ is the reduced energy given by

$$\epsilon = \frac{0.03255}{Z_1 Z_2 \left({Z_1}^{2/3} + {Z_2}^{2/3}\right)^{1/2}} \frac{M_1}{M_1 + M_2} E_{\mathrm{i}}, \tag{4.9}$$

Γ is a factor given as

$$\Gamma = \frac{W}{1 + (M_1/7)^3}, \tag{4.10}$$

where W is a dimensionless parameter that can be found in Yamamura and Tawara's paper.[39] k_{e} is the Lindhard electronic stopping coefficient which is given as

$$k_{\mathrm{e}} = 0.079 \frac{(M_1 + M_2)^{3/2}}{{M_1}^{3/2} {M_2}^{1/2}} \frac{{Z_1}^{2/3}\, {Z_2}^{1/2}}{\left({Z_1}^{2/3} + {Z_2}^{2/3}\right)^{3/4}}. \tag{4.11}$$

Since the dominant component of stainless steel is iron, atomic number 26, we are able to take iron as stainless steel in the calculation for simplicity. Tables 4-3 and 4-4 show the values that have been used in this thesis.

Table 4-3. Threshold energy of different incident atom on target atom[6,40]

Incident Atom/Target Atom	Threshold Energy [eV]
Xenon/Molybdenum	48
Argon/Stainless Steel	22.35

Table 4-4. Properties of different atoms

Atom	Atomic Mass [amu]	Atomic Number
Xenon	131.293	54
Argon	39.948	18
Molybdenum	95.96	42
Stainless Steel	55.845	26

To make the comparison between different thrusters more precise, we present the sputtering yield for xenon on molybdenum with Equation (4.3) instead of Equation (2.26). These two equations are estimated from different empirical data, so the fitting curves are slightly different as shown in Figure 4-5.

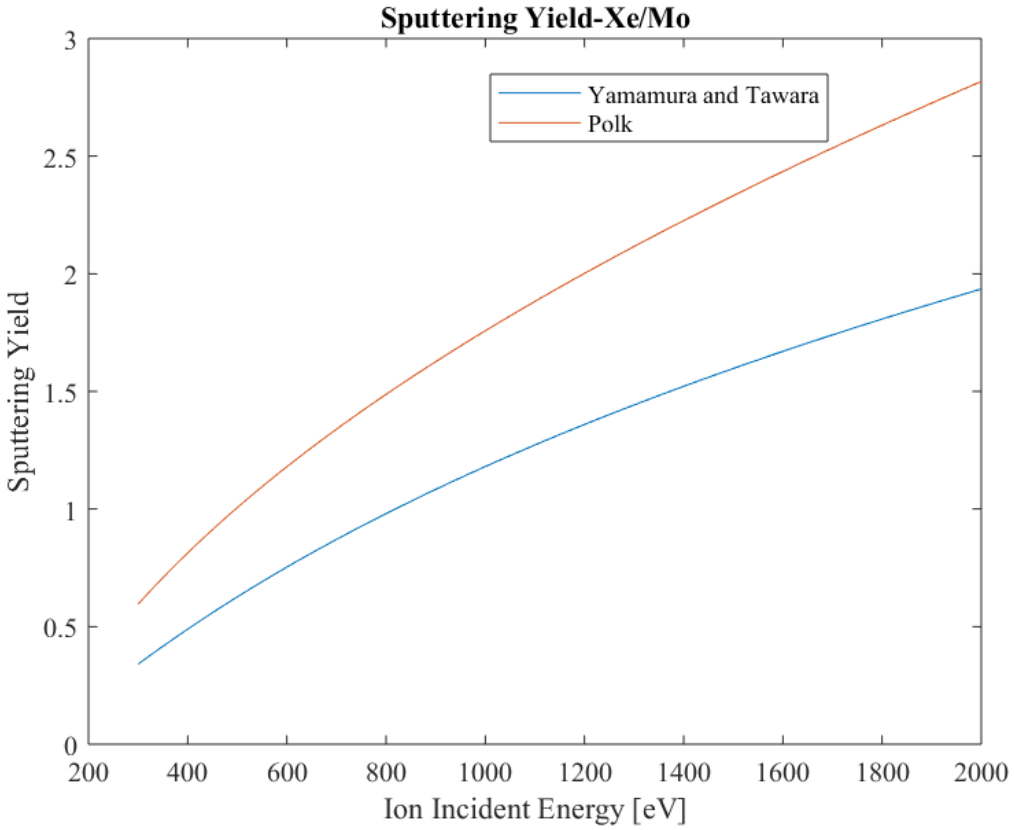

Figure 4-5. Ion incident energy vs. sputtering yield for Xe on Mo

Figure 4-6 shows the hole diameter and the corresponding K value. In this figure, we vary the hole diameter and fixed the other parameters in the K equation. The initial hole diameter (red

plus) and hole diameter after operating (red circle), which is the average of all the holes. The *K* value corresponds to the average hole diameter after running the thruster.

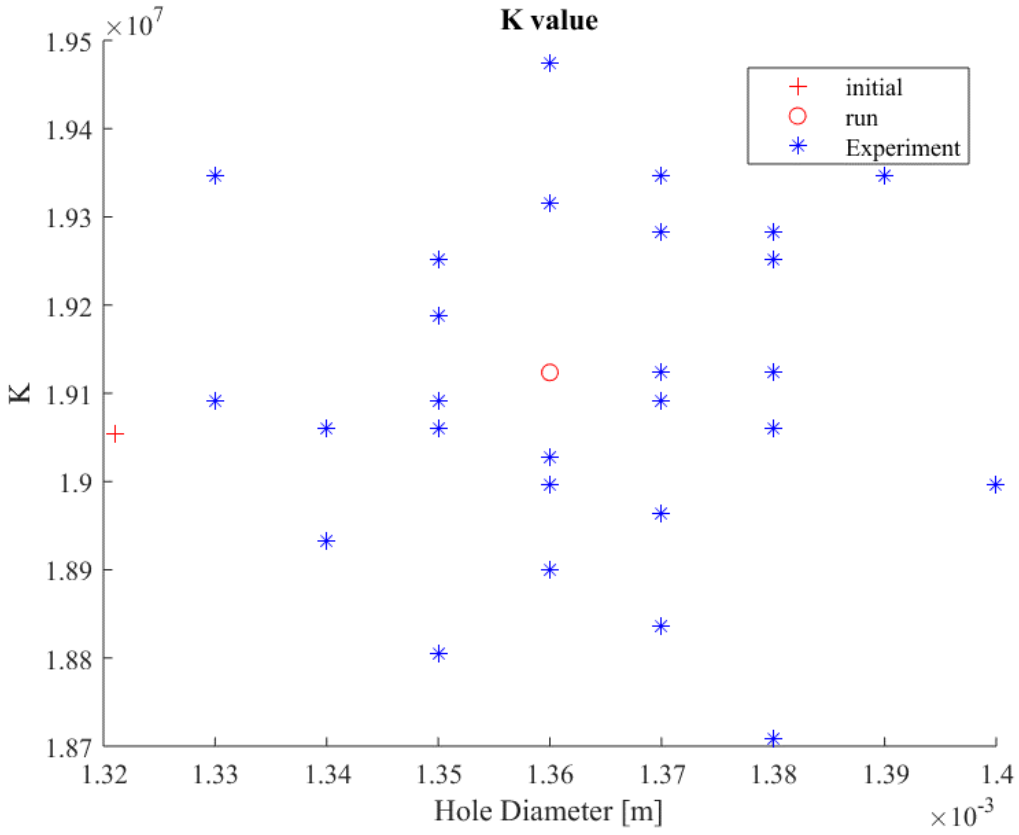

Figure 4-6. Experimental data of hole diameter vs. *K*

In Figure 4-7 the red plus represents the initial *K* value of the latest thruster. The red line and blue line stand for the *K* values after operation. The lines represent the predicted *K* value with the increase of the hole diameter. As shown in Figure 4-7, the *K* value will increase with the hole diameter. The increase in the hole diameter will result in a larger ion beam active area. The larger beam active area will increase the space for ions to pass through the grid; however, this will also decrease the area for generating the electric field. The increase in the voltage difference can cover the loss of the effective area of the electric field.

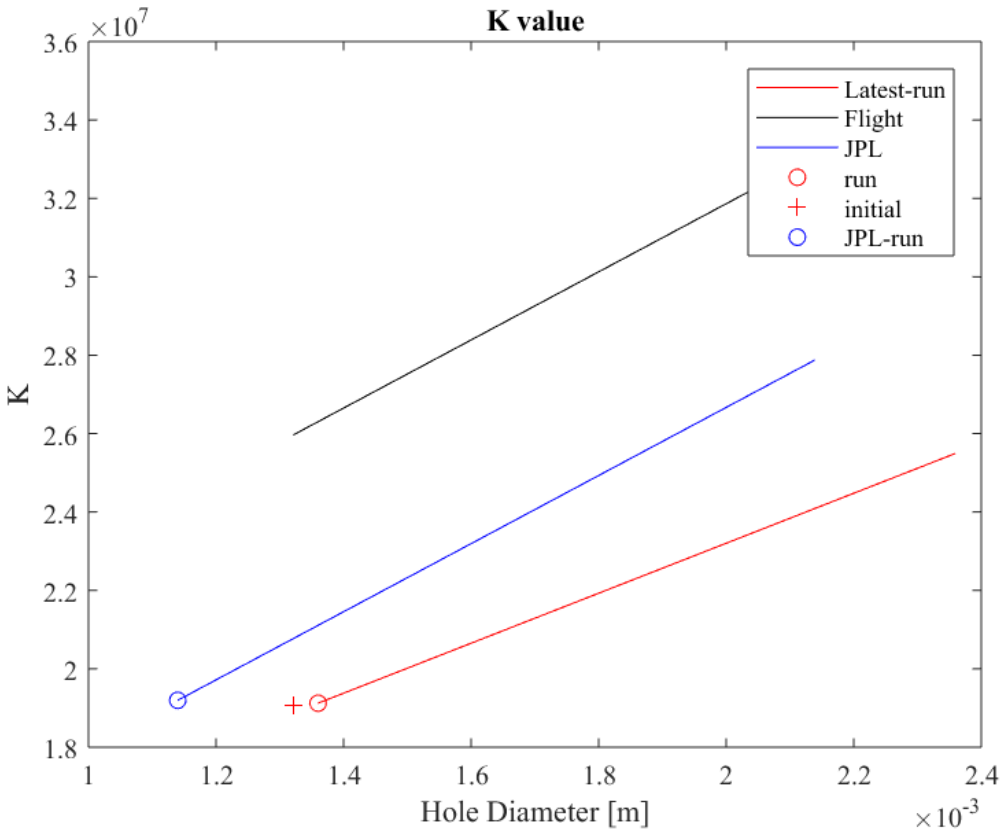

Figure 4-7. Hole diameter vs. *K*

Increasing the voltage might address the loss from a larger hole diameter; however, the increased voltage will also lead to sputtering. In the MMIT, we assume the ion incident energy is mainly provided by the voltage between the grids. Sputter yield can be calculated from Equation (4.3) for both xenon on molybdenum and argon on stainless steel. In Figure 4-8, the more voltage applied will cause more sputtering. Xenon has a lower ionization energy and higher atomic mass than argon; hence, previous research suggests the flight version should use xenon and molybdenum. However, the sputtering yield for xenon on molybdenum has greater effect than argon on stainless steel at high incident energy, as shown in Figure 4-8. The high incident energy results from the high applied voltage. The high voltage provides higher speed for ions and, hence, higher thrust. But, the high applied voltage will cause the greater sputtering of xenon on molybdenum and reduce grid life.

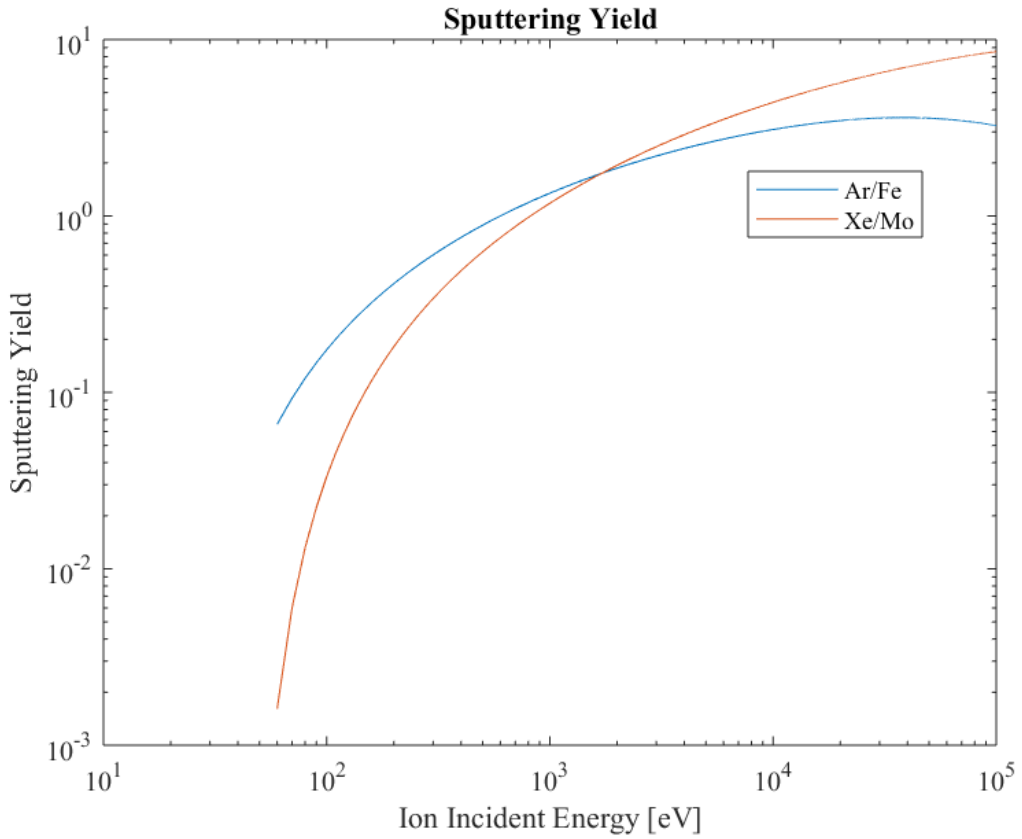

Figure 4-8. Ion incident energy vs. net sputtering yield for Xe on Mo and Ar on Fe

The voltage difference functions as the throttle in the MMIT. There exists the limitation on the voltage since EP is power limited. To understand the relation between voltage and K, we vary the voltage and fixed the other parameters in the K equation. The results in Figure 4-9 represent the flight version with the same deformation as the latest thruster prototype. As shown in Figure 4-9, the K value decreases with increasing voltage. Figure 4-10 shows the comparison among these thrusters. The K value is higher after operation in both the flight thruster and the latest thruster prototype because the starting hole diameter after expanding is larger than the initial hole diameter. We mentioned voltage can help us reduce the disadvantage due to a larger beam active area. However, the higher voltage coincides with the lower K value.

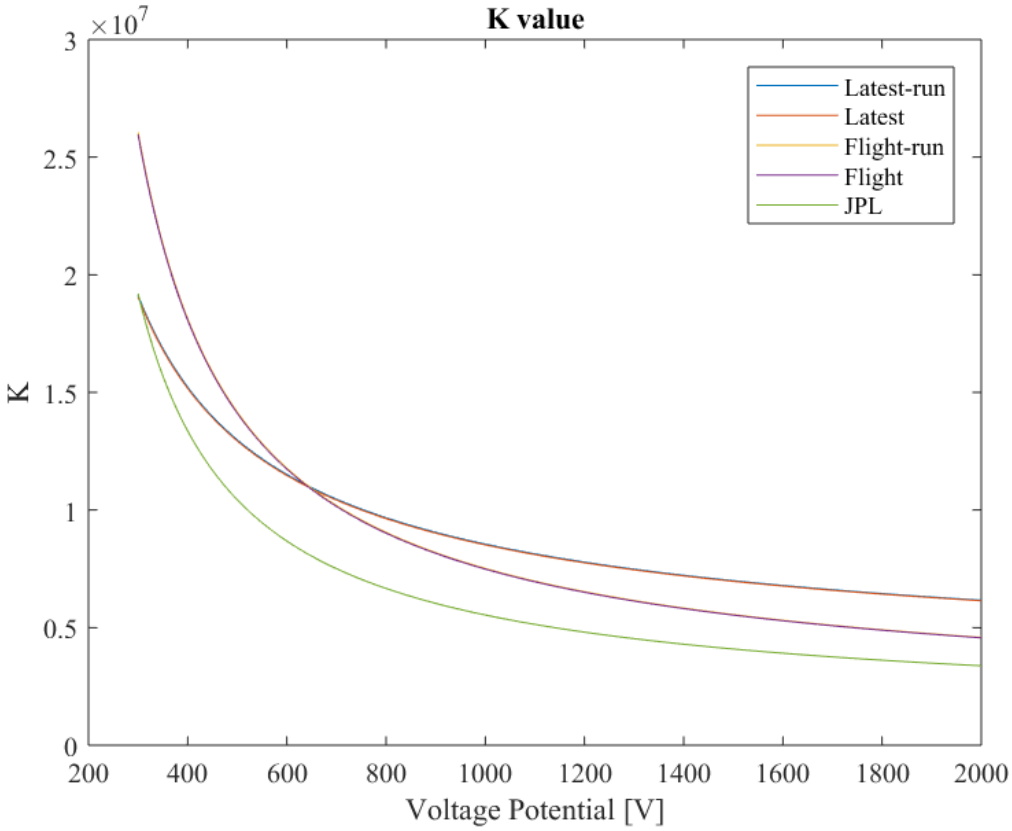

Figure 4-9. Voltage vs. *K*

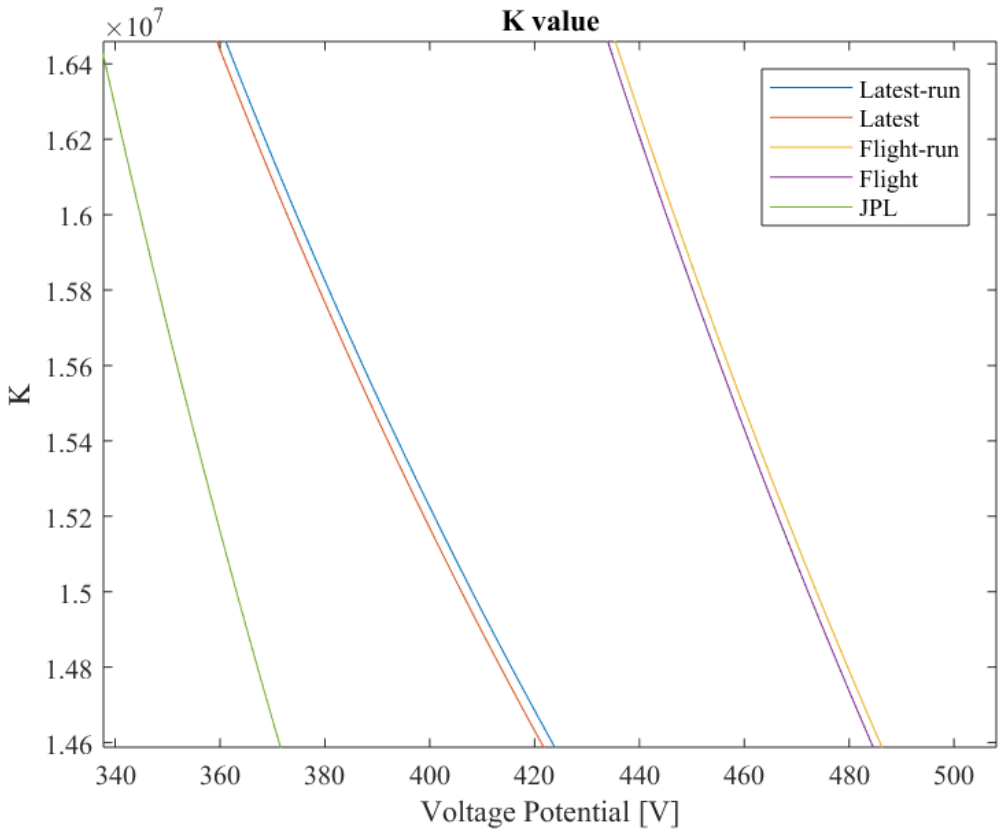

Figure 4-10. Voltage vs. K – partial view

4.5 New Design Criterion

There are two determining factors for K that we have discussed: deformation and voltage. The experimental data on deformation has been provided and these data show the increase in hole diameter. These findings are related to the thrust because, according to Equation (2.3), the MMIT thrust is a function of the number of and how fast the ions are going through the grids. The velocity of the ions depends on the voltage difference between the two grids, Equation (2.9). Thus, thrust is related to the hole diameter and voltage difference. The tradeoff between these two parameters is they are correlated and with the K value. There is a voltage limitation since EP is power limited. Therefore, we conclude that there exists a threshold value of hole diameter, which should not be too high to detrimentally affect the electric field nor too small to lessen the K value. The sputtering yield for different grid material and propellants correlated with the voltage limitation. Therefore, grid material and propellant should be determined by the thrust and life requirement for different

missions. Based on the findings above, a new design criterion has been established on the hole diameter.

Chapter 5

Conclusions and Future Work

Previous research highlighted arcing and sputtering issues with the MMIT, which caused damage to the grid. To determine how this damage affects the thruster's performance, in this thesis we studied the grid life, which is determined by the mass loss rate of the grid. Based on Polk's equations, we defined a new parameter, K, representing the known values in the life equation. The experimental data show that the hole diameter increases after running the thruster for a period of time. The energetic ions bombarding the grid material cause sputtering. Those energetic ions are generated by the electric field in the acceleration process. From the experimental data, we analyzed the relationships of the hole diameter and voltage with K. The relationship between the hole diameter and the voltage can affect the thrust. In EP, thrust can be determined by the number of ions extracted and the velocity of the exhaust ions. The larger hole diameter gives a larger space for ion extraction. However, the decreased grid area will weaken the electric field. The increase of voltage can cover the loss from hole expansion.

Previous design methodology for the grids was based on the thrust requirement. As we find in the research of grid life, hole diameter and voltage play important roles in determining thrust. In the analysis we presented, the hole diameter and voltage have relative effects on K. The hole diameter is also related to voltage. We cannot define which parameter is more significant to either life or thrust. However, previous design guidelines do not include the life effect. To design a fully functional fight version of thruster, the design guideline should include the grid life.

Suggestions for future work that will drive the next prototype iteration during the development of the MMIT are:

- Sputtering yield: The analytical formulas of sputtering yield presented in the thesis are only two of many approximations. A more accurate prediction and analysis should be found or experimentally determined.
- Uncertainties: The uncertainties in the life equation are hard to define because they change over time. However, a statistical analysis can help predict the failure rate. The uneven deformation could be large enough to bend the grid. The bending of the grid causes leakage

in the discharge chamber and might increase the chance of arcing. Therefore, the shape factor in the uncertainties needs to be defined.

- Other life factors
    - Pressure: Although the pressure difference between the chamber and the exhaust zone is small, there still exists the pressure difference. The pressure will affect the deformation and the breakdown voltage.
    - Heating: Since we apply electric current and electromagnetic waves to the thruster, it is possible that heat will damage or change material properties.
    - Outgassing: The above analysis did not include outgassing, but outgassing will contaminate the thruster and possibly cause failure.
- Build-up material: More research on the tradeoff between thrust (high applied voltage) and life of grid (sputtering yield) can help determine the grid material and propellant used in the flight version of the MMIT.
- Particle simulation: The movement of the ions and electrons are significant for the thruster. Understanding of the particle dynamics can help in optimizing the electron cyclotron resonant zone and ion extraction, and possibly help to design a grid that switches between the ion extraction mode and the neutralization mode.[21]

Bibliography

[1] Kaufman, H., *An Ion Rocket with an Electron-Bombardment Ion*, 1961.

[2] Jahn, J., Robert G., *Physics of Electric Propulsion*, McGraw-Hill, 1968.

[3] "Deep Space 1" Available: http://www.jpl.nasa.gov/missions/deep-space-1-ds1/.

[4] Sengupta, A., Anderson, J. A., Garner, C., Brophy, J. R., Groh, K. D., Banks, B., and Karniotis, T. A., "Deep Space 1 Flight Spare Ion Thruster 30,000-Hour Life Test," *Journal of Propulsion and Power*, vol. 25, Jan. 2009, pp. 105–117.

[5] Moore, N., Ebbeler, D., and Creager, M., "A Methodology for Probabilistic Prediction of Structural Failures of Launch Vehicle Propulsion Systems," American Institute of Aeronautics and Astronautics, 1990.

[6] Polk, J. E., Moore, N., Newlin, L., Brophy, J. R., and Ebbeler, D., "Probabilistic Analysis of Ion Engine Accelerator Grid Life," 1993.

[7] Ira, K., Polk, J., Brophy, J., and Anderson, J., "Numerical Simulations of Ion Thruster Accelerator Grid Erosion," American Institute of Aeronautics and Astronautics, 2002.

[8] Wang, J., Polk, J., Brophy, J., and Katz, I., "Three-Dimensional Particle Simulations of Ion-Optics Plasma Flow and Grid Erosion," *Journal of Propulsion and Power*, vol. 19, Nov. 2003, pp. 1192–1199.

[9] Emhoff, J., and Boyd, I., "Grid Erosion Modeling of the Next Ion Thruster Optics," American Institute of Aeronautics and Astronautics, 2003.

[10] Tartz, M., and Neumann, H., "Validated Ion Thruster Grid Lifetime Simulation," American Institute of Aeronautics and Astronautics, 2006.

[11] Wang, Y., Tang, H., Liu, C., Wang, H., Gu, Z., and Guo, N., "Life Tests and Measurements of Ion Thruster Accelerator Grid Erosion," American Institute of Aeronautics and Astronautics, 2008.

[12] Miyasaka, T., Kobayashi, T., and Asato, K., "Numerical Prediction of Grid Erosion of Ion Engine," *Transactions of The Japan Society for Aeronautical and Space sciences, Aerospace Technology Japan*, vol. 8, 2010, p. Pb_61-Pb_66.

[13] Masakatsu, N., "Simulations and Visualizations of Grid Erosion in Ion Engines," 2010, p. 4.

[14] Nakano, M., "Numerical Analysis for Highly Eroded Grid Surfaces of μ20 Ion Engine," *The Japan Society for Aeronautical and Space Sciences, Aerospace Technology Japan*, vol. 10, 2012.

[15] Nakano, M., and Koizumi, H., "Grid Wear Analysis of a Miniature Ion Engine," International Electric Propulsion Conference, 2015.

[16] Hill, P. G., and Peterson, C. R., *Mechanics and Thermodynamics of Propulsion*, Addison-Wesley, 1992.

[17] Leiter, H. J., Killinger, R., Bassner, H., Müller, J., and Kukies, R., "Development of the Radio Frequency Ion Thruster RIT XT – A Status Report," p. 8.

[18] Takao, Y., Koizumi, H., Komurasaki, K., Eriguchi, K., and Ono, K., "Three-dimensional Particle-in-cell Simulation of a Miniature Plasma Source for a Microwave Discharge Ion Thruster," *Plasma Sources Science and Technology*, vol. 23, Dec. 2014, p. 064004.

[19] Trudel, T. A., Bilén, S. G., and Micci, M. M., "Design and Performance Testing of a 1-cm Miniature Radio-frequency Ion Thruster," *The 31st International Electric Propulsion Conference*, 2006, p. 6.
[20] Mistoco, V. F., *Modeling of Small Scale Radio-frequency Inductive Discharges for Electric Propulsion Applications*, Ph.D. Dissertation, The Pennsylvania State University, 2011.
[21] Koizumi, H., and Kuninaka, H., "Ion Beam Extraction and Electron Emission from the Miniature Microwave Discharge Ion Engine μ1," *International Electric Propulsion Conference, IEPC-2009-178*, 2009.
[22] Lubey, D. P., "Development of a Miniature Microwave-Frequency Ion Thruster," M.S. Thesis, 2011.
[23] Lubey, D. P., Bilén, S. G., Micci, M. M., and Taunay, P.-Y., "Design of the Miniature Microwave-frequency Ion Thruster," *Proc. 32nd Int. Electr. Propuls. Conf.*, 2011, pp. 1–8.
[24] Taunay, P.-Y., "Testing and Optimization of a Miniature Microwave Ion Thruster," M.S. Thesis, 2012.
[25] Taunay, P.-Y. C., Bilén, S. G., and Micci, M. M., "Numerical Simulations of a Miniature Microwave Ion Thruster," *33rd Int. Elect. Propuls. Conf., Washington, DC, USA*, 2013.
[26] Asif, M., Bilén, S. G., and Micci, M. M., "Prototyping and Optimization of a Miniature Microwave-Frequency Ion Thruster," *35th International Electric Propulsion Conference*, Georgia Institute of Technology, USA: 2017, pp. 1–8.
[27] Asif, M., "Prototyping and Optimization of a Miniature Microwave-Frequency Ion Thruster," The Pennsylvania State University, M.S. Thesis, 2018.
[28] Patterson, M., and Verhey, T., "5 kW Xenon Ion Thruster Lifetest," American Institute of Aeronautics and Astronautics, 1990.
[29] Anderson, J. R., Polk, J. E., and Brophy, J. R., "Service Life Assessment for Ion Engines," International Electric Propulsion Conference, 1997, p. 8.
[30] Nakano, M., and Arakawa, Y., "Ion Thruster Lifetime Estimation and Modeling Using Computer Simulation," 1999.
[31] Funaki, I., Nakano, M., Kajimura, Y., Miyasaka, T., Nakayama, Y., Hyakutake, T., Wada, M., Kenmotsu, T., Muramoto, T., Kuninaka, H., and Shinohara, I., "A Numerical Tool for Lifetime Evaluation of Ion Thruster's Ion Optics," American Institute of Aeronautics and Astronautics, 2011.
[32] Funaki, I., Watanabe, H., Nakano, M., Kajimura, Y., Miyasaka, T., Nakayama, Y., Kuninaka, H., and Shinohara, I., "Numerical Lifetime Evaluation of Ion Thruster's Ion Optics Using the JIEDI Tool," American Institute of Aeronautics and Astronautics, 2012.
[33] Moore, N., Ebbeler, D., and Sutharshana, S., "Probabilistic Failure Risk Assessment for Structural Fatigue," 1993.
[34] Rosengaus, D., and Wehner, "Sputtering Yields for Low Energy He+-, Kr+-, and Xe+-Ion Bombardment," *Journal of Applied Physics*, vol. 33, May 1962.
[35] Hechtl, E., and Bohdansky, J., "Sputtering Behavior of Graphite and Molybdenum at Low Bombarding Engines," *Journal of Nuclear Materials*, 1984, p. 6.

[36] Stanford Research Systems, *"Series PS300 High Voltage Power Supplies - User Manual"*, 2007.
[37] "Newport, "Oriel 70705 High Voltage Power Supply - Datasheet" Available: https://www.artisantg.com/info/ATGpmqhw.pdf.
[38] "Bearing Electronic LCD Digital Vernier Caliper Measuring Tool," *VXB.com Bearings* Available: https://www.vxb.com/product-p/kit7426.htm.
[39] Yamamura, Y., and Tawara, H., "Dependence of Ion-Induced Sputtering Yields From Monatomic Solids at Normal Incidence Energy," *Atomic Data and Nuclear Data Tables*, vol. 62, Mar. 1996, pp. 149–253.
[40] Matsunami, N., Yamamura, Y., Itikawa, Y., Itoh, N., Kazumata, Y., Miyagawa, S., Morita, K., Shimizu, R., and Tawara, H., "Energy Dependence of the Ion-induced Sputtering Yields of Monatomic Solids," *Atomic Data and Nuclear Data Tables*, vol. 31, Jul. 1984, pp. 1–80.